

# Filtering method in backlash phenomena analysis

Miguel F.M. Lima, J.A. Tenreiro Machado, Manuel Crisóstomo

## ABSTRACT

The behavior of robotic manipulators with backlash is analyzed. Based on the pseudo-phase plane two indices are proposed to evaluate the backlash effect upon the robotic system: the root mean square error and the fractal dimension. For the dynamical analysis the noisy signals captured from the system are filtered through wavelets. Several tests are developed that demonstrate the coherence of the results.

Keywords: Backlash, Robotics, Wavelets, Pseudo-phase plane, Fractal dimension

## 1. Introduction

The backlash phenomenon is found in many physical systems. This problem is particularly important in robotic manipulation where a high precision is needed. In fact, the backlash is one of the most important nonlinearities that limits the performance of the mechanical manipulators. This nonlinear dynamic phenomenon is an area of active research, but due to its complexity well established conclusions are still lacking.

The backlash in mechanical systems has two main aspects: the identification and the control. Several authors addressed the problem of identification [3–5,8,13,17,20,24]. Dagalakis and Meyers [3–5] proposed a technique based on the coherence function to detect backlash in robotic systems. The coherence function was calculated between the motor voltage and the velocity, or the acceleration of the arm, for a joint excitation with band limited random signals. The coherence function was shown to be a maximum at zero backlash and to drop in magnitude as the gear meshing decreases. Another technique proposed by Stein and Wang was based on the analysis of momentum transfer, to detect backlash in mechanical systems [20]. The change in the speed of the primary gear, due to impact with the secondary gear, is related to the magnitude of the backlash. The efforts towards the backlash detection include others' techniques such as artificial intelligence schemes and state space observers [8,13]. Trendafilova and Brussel [24] presented also a set of tools to analyze and monitor the nonlinear dynamics of the robot joints.

To mitigate the effects of the backlash, several authors have studied the aspect of controlling the mechanical systems with this nonlinearity [2,10,15]. Nordin and Gutman presented a survey of the techniques used to control the mechanical systems with backlash. The techniques included the use of linear controllers, state feedback and observer based algorithms. A control using the describing function, that is a common method for the analysis and synthesis of nonlinear systems, was



The manipulator is a vertical articulated robot with five rotational joints. The third joint connects the upper arm to the forearm of the robot. This joint is driven through a servomotor coupled to the harmonic drive gear by a timing belt. By adjusting the belt tension of the third joint two-stage transmission, three distinct degrees of backlash were introduced that are qualitatively classified as: (i) low backlash, (ii) medium backlash, (iii) high backlash. The vibration response is measured with two accelerometers. The accelerometers 1 and 2 are mounted in the end of the upper arm and forearm, respectively (see Fig. 1). The robot motion is programmed in a way such that only the third joint is driven, and consequently it oscillates, over a predefined range from the vertical position. The axis of the rotational joints 2, 3 and 4 are parallel; therefore, the effects

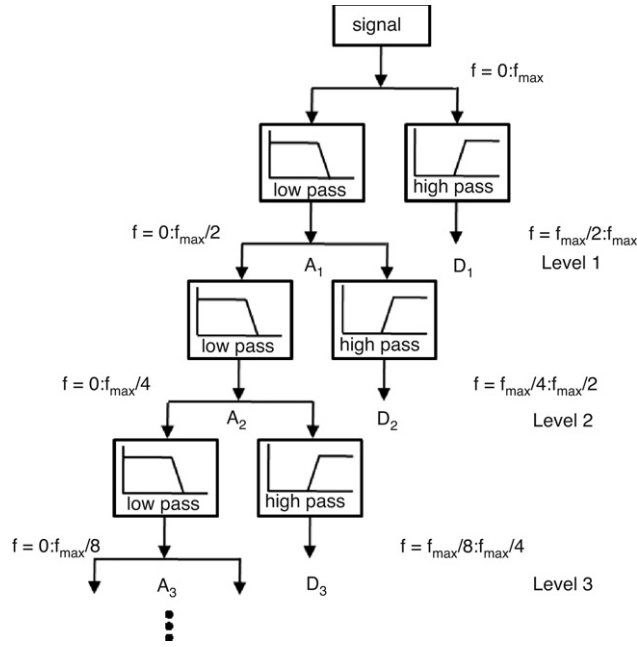


Fig. 2. Simplified diagram of a signal wavelet multiresolution analysis.

of the third axis rotation affect directly the adjacent joints. During the motion several signals are recorded with a sampling frequency of  $f_s = 750$  Hz. The signals come from different sensors, such as accelerometers, wrist force and torque sensor, position encoders and joint actuator current sensors. Fig. 1 (right) depicts the accelerometers mounted on the robot arm.

### 3. Main concepts

This section presents a review of the fundamental concepts involved in the experiments. In order to tackle the noisy signals captured by the accelerometers the de-noise capabilities of wavelets [12] are used. Additionally, the system behavior with backlash is analyzed through the pseudo-phase space [24].

#### 3.1. The wavelet transform

The continuous wavelet transform (CWT) is a generalization of the WFT. The concept of the WFT is very simple. We multiply the signal to be analyzed  $x(t)$ , by a moving window  $g(t - \tau)$ , and then we compute the Fourier transform of the windowed signal  $x(t)g(t - \tau)$ . Each FT gives a frequency domain 'slice' associated with the time value at the window centre. Wavelet analysis is performed in a similar way, in the sense that the signal is multiplied by a function called wavelet. However, in the CWT the width of the 'window' changes as the transform is computed. Diminishing the width reduces the frequency resolution and increases the time resolution. Augmenting the width has the opposite effect. Considering the wavelet function  $\psi$  centred at time  $\tau$  and scaled by  $s$ , the CWT of the signal  $x(t)$  is represented analytically by:

$$CWT(s, \tau) = \frac{1}{\sqrt{|s|}} \int_{-\infty}^{+\infty} x(t) \psi\left(\frac{t - \tau}{s}\right) dt. \quad (1)$$

The CWT of the signal  $x(t)$  is a function of two variables: translation  $\tau$ , that corresponds directly to time, and scale/dilation  $s$ , that indirectly relates to frequency information. The transforming function  $\psi(t)$  is called mother wavelet, and consists in a prototype for generating the other window functions. The translation  $\tau$  is related to the location of the window that is shifted through the signal. Therefore, this term corresponds to time information in the transform domain. The scale  $s$ , in the wavelet transform, is similar to the scale used in maps. High scales give a global view of the signal, corresponding in the frequency domain to the low frequencies. Low scales give detailed information of a signal, corresponding in the frequency domain to the high frequencies.

For a given mother wavelet, the CWT computation starts with  $s = s_1$ . Then the wavelet at this scale is shifted to the right by  $\tau$  amount up to the instant  $t = \tau$  and expression (1) is computed to obtain the transform value at  $(s, t) = (s_1, \tau)$ . This procedure is repeated until the end of the signal is reached. One row of points on time-scale plane for the scale  $s = s_1$  is then completed. The wavelet computation continues for all adopted values of  $s$ .

The digital version of the CWT is the discrete wavelet transform (DWT), that is considerably faster to implement in a computer. A time-scale representation of a digital signal can also be implemented using digital filtering techniques. An

efficient way to implement the DWT using filters was developed by Mallat [11]. Filters of different cut-off frequencies are used to analyze the signal at different scales (see Fig. 2). The signal is passed through a bank of high pass filters to analyze the high frequencies giving detailed information. Additionally, the signal is passed through a bank of low pass filters to analyze the low frequencies giving a coarse approximation. In resume, the details ( $D_n$ ) are the low-scale, high-frequency components and the approximations ( $A_n$ ) are the high-scale, low-frequency components of the signal. Then the decomposition of the signal into different frequency bands is obtained by successive high-pass and low-pass filtering of the time domain signal.

In what concerns to the wavelet function  $\psi(t)$  there are a wide variety of wavelet families proposed by different researchers that includes the Haar, Daubechies, Mexican Hat and Morlet wavelets. The function  $\psi(t)$  should reflect the type of features present in the time series [23]. Therefore, the wavelet adopted in this paper is the Haar (Eq. (2)) function due also to its simplicity and small computational time.

$$\psi(t) = \begin{cases} 1 & 0 \leq t < 1/2 \\ -1 & 1/2 \leq t < 1 \\ 0 & \text{otherwise.} \end{cases} \quad (2)$$

The wavelets have a wide variety of applications [12,22,25] in mathematics, physics and engineering. In this work we use the signal processing capabilities of the wavelets for de-noising the experimental signals.

### 3.2. The pseudo-phase plane

The pseudo-phase space (PPS) is used to analyze signals with nonlinear behavior. For the two-dimensional case it is called pseudo-phase plane (PPP) [1,7,24]. The proper time lag  $T_d$ , for the delay measurements, and the adequate dimension  $d \in N$  of the space must be determined in order to achieve the phase space. In the PPP the measurement  $s(t)$  forms the *pseudo-vector*  $y(t)$  according to:

$$y(t) = [s(t), s(t+T_d), \dots, s(t+(d-1)T_d)]. \quad (3)$$

The vector  $y(t)$  can be plotted in a  $d$ -dimensional space forming a curve in the PPS. There is a one-to-one relationship between the data in the PPS and the associated data in the true state space. If  $d = 2$  we have a two-dimensional time delay space. Therefore, the plot of PPP will not change substantially, since  $\{s(t), s(t+T_d)\}$  is related with  $\{s(t), \dot{s}(t)\}$ . In resume, we expect the PPP to preserve the major properties of the state space representation and, thus, to allow us to draw conclusions about the system dynamics.

The procedure of choosing a sufficiently large  $d$  is formally known as embedding and any dimension that works is called an embedding dimension  $d_E$ . The number of measurements  $d_E$  should provide a phase space dimension, in which the geometrical structure of the plotted PPS is completely unfold, and where there are no hidden points in the resulting plot.

In Eq. (3), if we choose  $T_d$  too small, then the time series  $s(t)$  and  $s(t+T_d)$  will be so close to each other (in numerical terms) that we cannot distinguish them. From a practical point of view they have not provided us with two independent coordinates. Similarly, if  $T_d$  is too large, then  $s(t)$  and  $s(t+T_d)$  are completely independent of each other (in a statistical sense) and the resulting time series present totally unrelated directions.

Among others [7], the method of delays is the most common method for reconstructing the phase space. Several techniques have been proposed to choose an appropriate time delay [1]. One line of thought is to choose  $T_d$  based on the correlation  $R$  of the time series with its delayed image. The correlation provides a measurement of the similarity between two time series that leads to good results when the series have a linear relationship. When  $R$  is a minimum it indicates that the delay  $T_d$  will lead to the independency of the series  $s(t)$  and  $s(t+T_d)$ . The difficulty of correlation to deal with nonlinear relations leads to the use of the mutual information. This concept, from the information theory [19], recognizes the nonlinear properties of the series and measures their dependence. The mutual information for the two series of variables  $t$  and  $t+T_d$  is given by:

$$I(t, t+T_d) = \log_2 \frac{F_1\{s(t), s(t+T_d)\}}{F_2\{s(t)\}F_3\{s(t+T_d)\}} \quad (4)$$

where  $F_1\{s(t), s(t+T_d)\}$  is a bidimensional probability density function and  $F_2\{s(t)\}$  and  $F_3\{s(t+T_d)\}$  are the marginal probability distributions of the two series  $s(t)$  and  $s(t+T_d)$ , respectively.

The average mutual information between the two time series is given by:

$$I_{av}(t, t+T_d) = \int_t \int_{t+T_d} F_1\{s(t), s(t+T_d)\} \log_2 \frac{F_1\{s(t), s(t+T_d)\}}{F_2\{s(t)\}F_3\{s(t+T_d)\}} dt d(t+T_d). \quad (5)$$

The index  $I_{av}$  allows us to obtain the time lag required to construct the pseudo-phase space. For finding the best value  $T_d$  of the delay,  $I_{av}$  is computed for a range of delays and the first minimum is chosen (widely referred in the literature thought not clearly). This procedure leads to the selection of the delay  $T_d$  corresponding to two time series that have a minimal mutual information, and, hence, to an optimal independence without excessively large delays. Usually  $I_{av}$  is referred [1,7,24] as the preferred alternative to select the proper time delay  $T_d$ .

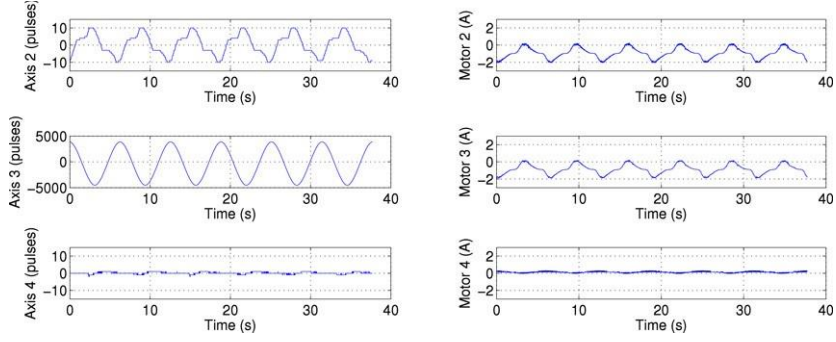


**Fig. 3.** Robot axis positions for joints 2–4 for the case (iii) (left) and electrical currents of robot axis motors 2–4 for the case (i) (right).

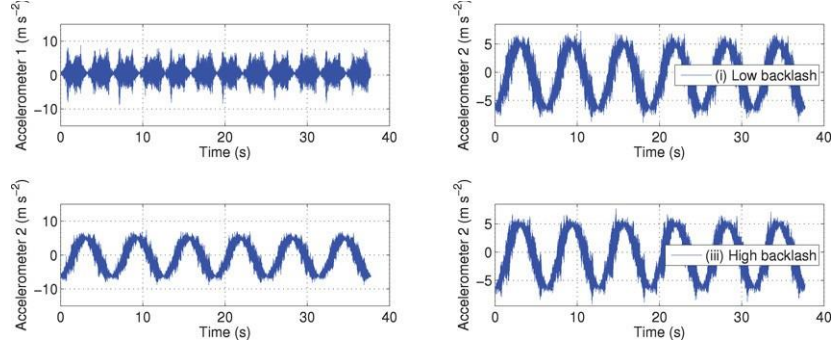


**Fig. 4.** Robot accelerations for the case (ii) (left) and robot accelerations for the cases (i) and (iii) (right).

### 3.3. The fractal dimension

The fractal dimension,  $D_F$ , is a quantity that gives an indication of how completely a spatial representation appears to fill space. There are many specific methods to compute the fractal dimension [6,16]. The most popular methods are the Hausdorff dimension and box-counting dimension. Here the box-counting dimension method is used due to its simplicity of implementation.

The fractal dimension is defined as:

$$D_F = \lim_{\epsilon \rightarrow 0} \frac{\ln [N(\epsilon)]}{\ln(1/\epsilon)}. \quad (6)$$

where  $N(\epsilon)$  represents the minimal number of covering cells ( $\epsilon$ , g., boxes) of size  $\epsilon$  required to cover a set  $S$ . The slope on a plot of  $\ln[N(\epsilon)]$  versus  $\ln(1/\epsilon)$  provides an estimate of the fractal dimension.

## 4. Results

According to the platform described in Section 2 we adopt an experiment in which the robot arm moves as a consequence of the joint 3 rotation. In other words, the robot motion is programmed in a way such that only the joint 3 is driven and, consequently, it oscillates over a predefined range from the vertical position.

Figs. 3 and 4 present a typical time evolution of some variables. All the captured robot signals (see Fig. 1 left) were studied but, due to space limitations, only the most relevant are depicted in this paper.

Fig. 3 (left) shows the axis positions of joints 2–4 for the case of high backlash. It is actuated only the joint 3, but due to the dynamic coupling, the adjacent joints 2 and 4 oscillate slightly. Fig. 3 (right) depicts the electrical currents of robot axis motors 2–4 for the low backlash (case i). The currents of the motors reveal the action of the robot control system ensuring the position control.

Fig. 4 (left) shows the robot accelerations for the case (ii). As referred previously, the accelerometers 1 and 2 are mounted in the end of the upper arm and forearm, respectively (see Fig. 1). The signals from the accelerometers present a considerable noise and it is difficult to extract information about the backlash. Several tests demonstrated that the effects of the adjusted backlash are captured only by the accelerometer 2. Although the signals from the other sensors present significant less noise, when compared with the accelerometers, the backlash is not observed by them. Moreover, due to the amount of noise the accelerometer 1 does not capture the backlash too.

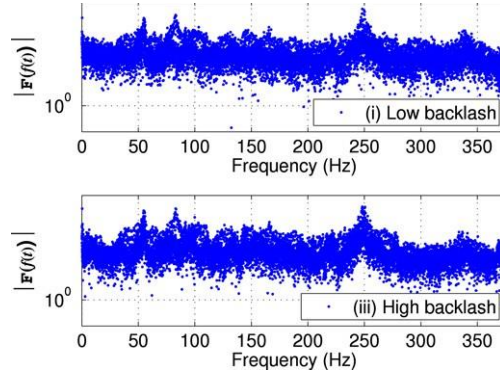


Fig. 5. Spectra of the accelerometer 2 signal.

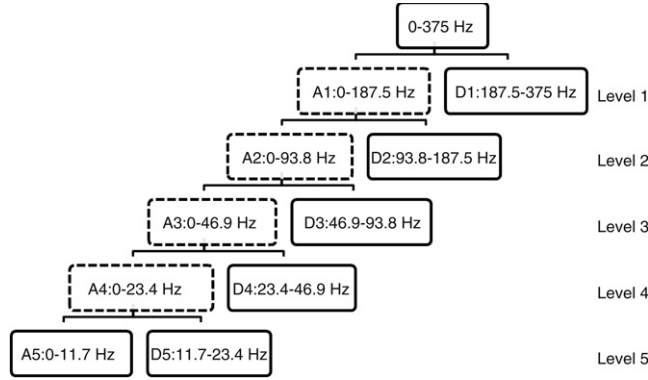


Fig. 6. Wavelet decomposition and the resulting frequency bands.

Fig. 4 (right) depicts the signal from the accelerometer 2 for the cases (i) and (iii). The signal corresponding to the case (iii) exhibits larger negative peaks compared with the case (i). In spite of this detail, it seems difficult to analyze the effect of the backlash from this noisy signal. Fig. 5 shows the spectrum of the accelerometer 2 signal for the cases (i) and (iii). Both spectra are identical which confirms the undesirable result of the noise that hides the backlash. Therefore, to analyze the backlash the signals must be filtered. First, it was tried a low pass Butterworth filter versions with different cut-off frequencies. The resulting filtered signal presented a noise reduction, but the backlash effect was not yet clear. As an alternative the wavelets were adopted. Preliminary tests, with several wavelet families, were performed to verify their capabilities. The Haar wavelet revealed good results and was adopted due to its simplicity and low computational time.

Fig. 6 depicts the wavelet decomposition tree with the resulting frequency bands of the corresponding approximation ( $A_n$ ) and detail ( $D_n$ ) components for each level. Since the sampling rate of the captured signal is 750 Hz, the frequency ranges are approximately the values shown in the diagram.

Fig. 7 (left) shows the five level components obtained through the process of decomposition of the accelerometer 2 signal in the case (i). The original signal captured from the accelerometer 2 is shown at the top. The approximation component reveals the low frequency part of the acceleration 2. The five detail components show the high frequency parts for the different frequency bands. A method of filtering based on the threshold level for each component is used. For the distinct components, the values adopted for the threshold level are  $[3.68, 4.37, 4.21, 4.04, 3.87, 3.68] \text{ ms}^{-2}$ . Fig. 7 (right) shows at the top the resulted filtered signal. Now, the effect of the backlash is evident. Fig. 7 (right) shows also the six components of the filtered signal, corresponding to the same frequency bands shown in Fig. 7 (left). Comparing the five detail components of the filtered signal, with those ones from the original signal, it is clear the effect of filtering. The filtered periodic signal can be expanded to a Fourier series in the form:

$$x_{FS}(t) = a_0 + \sum_{k=1}^{+\infty} [a_k \cos(k\omega t) + b_k \sin(k\omega t)]. \quad (7)$$

An infinite number of terms (*i.e.*, the fundamental term and the harmonics) are required to fit the filtered signal  $x(t)$  with  $x_{FS}(t)$ . However, we can assume that the filtered signal  $x(t)$  (see Fig. 7 top-right) is composed by the fundamental harmonic perturbed by the backlash effect. Therefore for the low backlash (case i), with  $k = 1$ , we obtain  $(a_0, a_1, b_1) = (-0.59, -5.44, 0.64)$ . Fig. 8 shows the filtered accelerometer 2 signal for the case (i) and its fundamental harmonic.



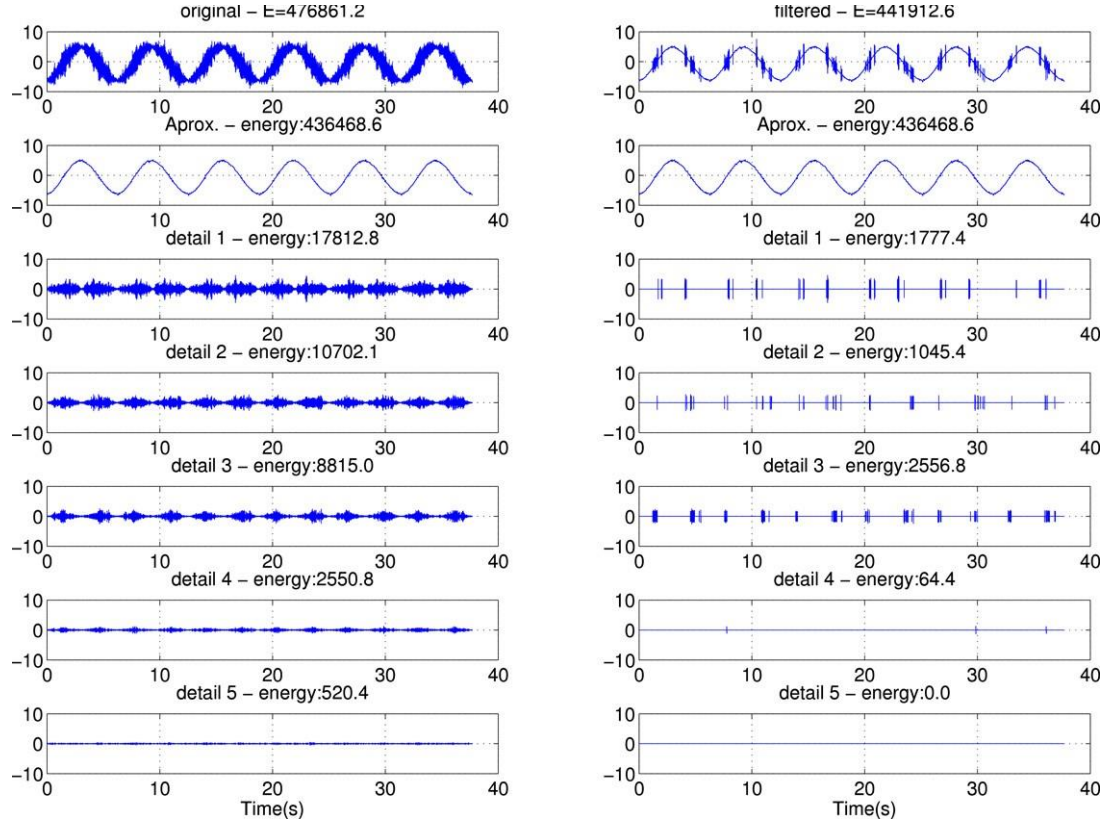


Fig. 7. Wavelet decomposition of the accelerometer 2 signal for the case (i): noisy (left); filtered (right).

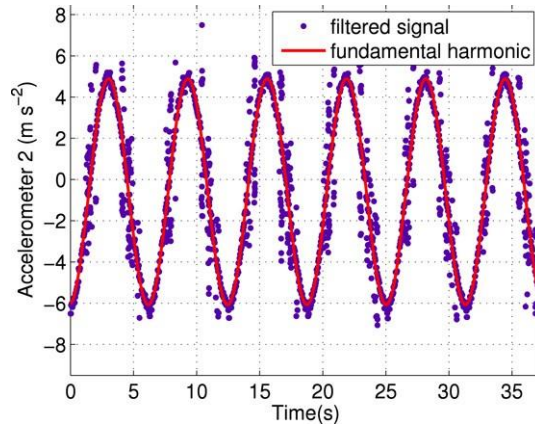


Fig. 8. Filtered accelerometer 2 signal and its fundamental harmonic for the case (i).

Fig. 9 depicts the PPP of the filtered accelerometer 2 signals for the experiment with the low and high backlash and their fundamental harmonic. As referred previously, usually the time lag adopted for the PPS is based on the correlation or mutual information of the time series. In this work, practice reveals that the best time lag is that one corresponding to one quarter of the period of the fundamental harmonic, which was adopted for the PPP shown in Fig. 9.

In order to analyze the influence of the distinct levels of backlash in the robotic system a metric based on the error between the filtered signal and its fundamental harmonic was developed. For the two components  $x(t)$  and  $x(t - T)$  of the PPP, the index is based on the root mean square error (RMSE) in discrete time given by:

$$\text{RMSE}^2 = \text{RMSE}_t^2 + \text{RMSE}_{t-T}^2 \quad (8)$$

where  $\text{RMSE}_t \{x(t)\} = \frac{\frac{1}{N} \sum_{k=0}^{N-1} [x(kT) - x_1(kT)]^2}{\frac{1}{N} \sum_{k=0}^{N-1} x_1^2(kT)}$ ,  $x_1(t)$  is the fundamental harmonic and  $T$  is the sampling period.

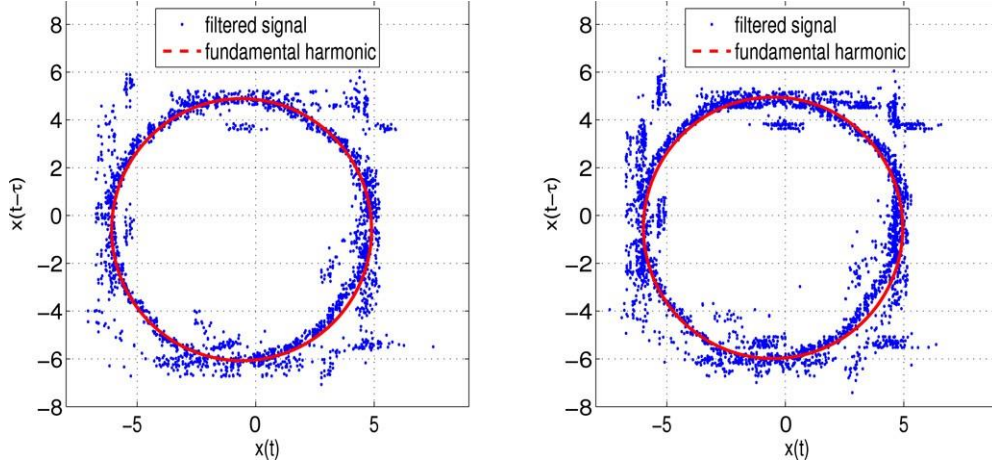


Fig. 9. PPP of the filtered accelerometer 2 signal and its fundamental harmonic for the cases: (i) low backlash (left); and (iii) high backlash (right).

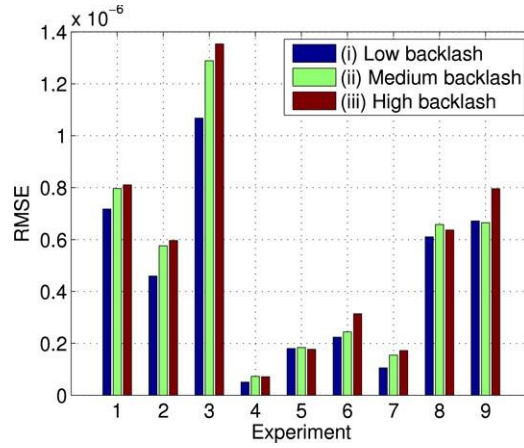


Fig. 10. RMSE of the accelerometer 2 signal for a set of experiments: cases (i), (ii) and (iii).

The RMSE values computed for the three cases of backlash  $(RMSE^i, RMSE^{ii}, RMSE^{iii}) = (0.46, 0.57, 0.59) \times 10^{-6}$  show that the index values increase with the level of the backlash. Additionally, a set of experiments were developed to study the influence of the amplitude and frequency of the joint 3 motion upon the backlash dynamics. Fig. 10 depicts the RMSE of the accelerometer 2 signal for the nine experiments.

The results confirm in general the behavior of the RMSE that increases with the degree of the backlash. However, the index is not in complete accordance with the expected results for some experiments. This fact can be caused by the noise of the signal that is not filtered completely, probably due to the method adopted for the selection of the threshold level. The use of another method (e.g., an heuristic one) or the use of another type of wavelet, could mitigate the problem of the noise. A deeper insight into the nature of this problem must be envisaged.

Additionally, Fig. 11 (left) depicts the RMSE values of the accelerometer 2 signal *vs* the amplitude and frequency of joint 3 movements for low backlash case. The nine points, shown in Fig. 10 for each individual case, form now a surface that relates the three variables demonstrating the existence of a smooth curve linking the variables. There is a maximum of  $RMSE = 1.06 \times 10^{-6}$  that occurs at (frequency, amplitude) = (0.6, 6.5). Fig. 11 (right) depicts the same variables as shown in the left, but for the high backlash case. There is a maximum of  $RMSE = 1.35 \times 10^{-6}$  that occurs again at the same values of (frequency, amplitude) = (0.6, 6.5).

The PPP has the ability to concentrate the data in the space, which facilitates the applicability of metrics based on geometric properties. In this perspective, the fractal dimension  $D_F$  (6) is also studied. Fig. 12 (left) shows the  $D_F$  values for the three cases. The  $D_F$  index gives almost similar values for the same experiment and, therefore, this index does not distinguish clearly the cases related to the backlash level. Fig. 12 (right) depicts, as an example, the  $D_F$  index *vs* the amplitude and the frequency of joint 3 movements for the medium backlash case. There is a minimum of  $D_F = 1.3$  that occurs at (frequency, amplitude) = (0.6, 6.5). Comparing the Fig. 11 (right) and Fig. 12 (right), the  $D_F$  index detects the general behavior of the backlash effect. Nevertheless,  $D_F$  presents a low resolution when detecting the three cases.



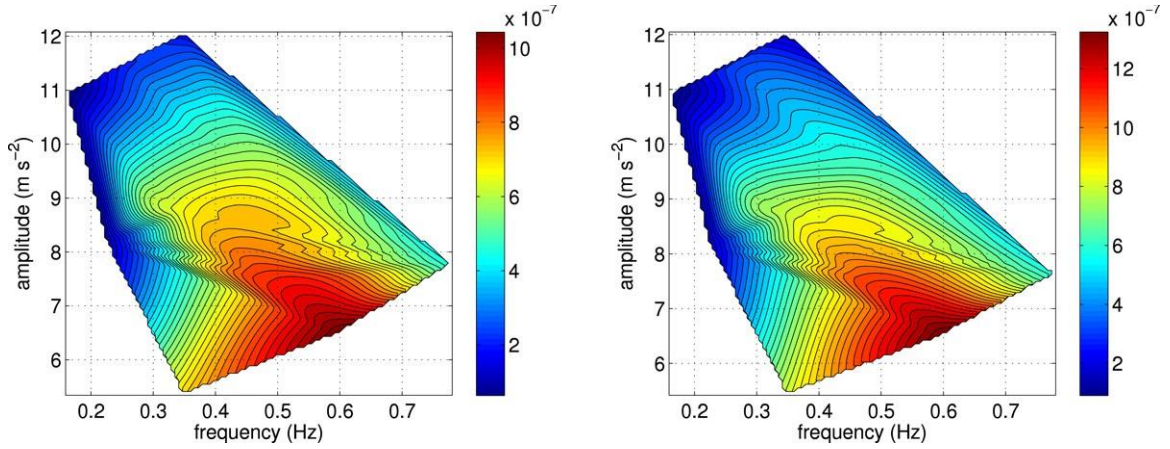


Fig. 11. RMSE of the accelerometer 2 signal *vs* amplitude and frequency of joint 3 movements for the cases (i) (left) and (iii) (right).

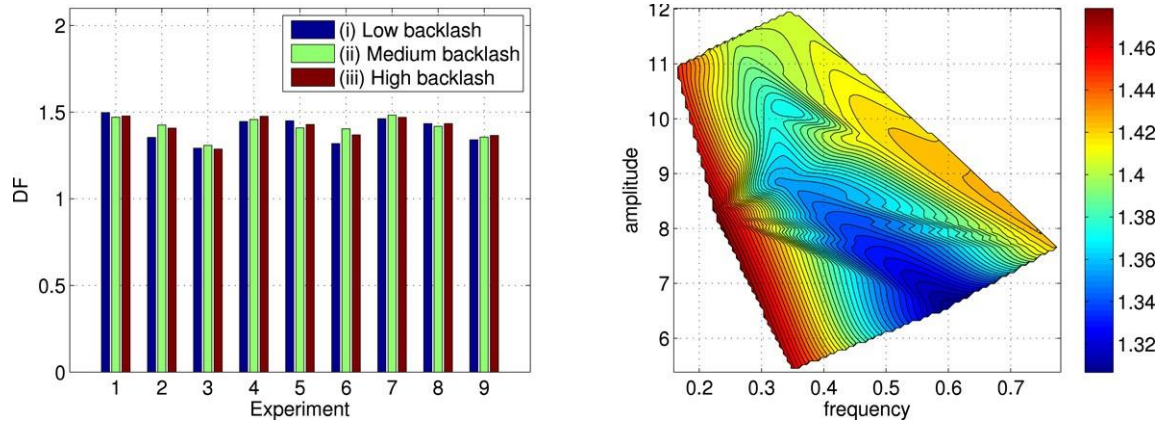


Fig. 12.  $D_F$  of the accelerometer 2 signal for the three cases of backlash (left) and  $D_F$  of the accelerometer 2 signal *vs* amplitude and frequency of joint 3 movement for the case (ii) (right).

In conclusion, the tests developed in this article proved that the RMSE is more sensitive, compared with the  $D_F$ , and, therefore, the RMSE reveals to be a good index for the backlash analysis. Additionally, the wavelets and the PPP revealed to be adequate tools for analyzing the backlash phenomena. In this line of thought, other analysis tools can be envisaged in the viewpoint of the wavelets and the PPP properties. In fact, from the wavelets decomposition new indices can be developed based on the amplitude of the relevant components. From the PPP graphical representation it is also possible to establish new criteria based on statistics and figure shape characteristics.

## 5. Conclusions

Several experiments demonstrate the effectiveness of the wavelets on filtering the experimental signals reducing the noise while maintaining important features about the backlash.

Two different indices were proposed to detect the backlash effect on a robotic manipulator, namely the RMSE and the  $D_F$ . While the RMSE reveals to be an appropriate index for the backlash analysis, the  $D_F$  presents a lower resolution which restricts its applicability.

In future work, we plan to pursue several researches to help us further understand the backlash phenomenon. These include the study of the wavelet tuning parameters, in the process of de-noising, and the analysis of the backlash with various static pre-loads applied on the robot end-effector. Other indices will also be developed.

## References

- [1] H.D.I. Abarbanel, R.R. Brown, J.J. Sidorowich, L.Sh. Tsimring, The analysis of observed chaotic data in physical systems, *Reviews of Modern Physics* 65 (4) (1993) 1331–1392.
- [2] Abilio Azenha, J.A. Tenreiro Machado, Variable structure control of robots with nonlinear friction and backlash at the joints, in: *Proc. of the IEEE Int. Conf. on Robotics and Automation*, 1996, pp. 366–371.

- [3] Nicholas G. Dagalakis, Donald R. Myers, Adjustment of robot joint gear backlash using the robot joint test excitation technique, *The International Journal of Robotics Research* (1985) 65–79.
- [4] Nicholas G. Dagalakis, Donald R. Myers, Adjustment of robot joint gears using encoder velocity and position information, *Journal of Robotic Systems* 2 (2) (1985) 229–234.
- [5] Nicholas G. Dagalakis, Donald R. Myers, Use of coherence analysis for the evaluation and adjustment of robot gear performance, *Robotics & Computer-Integrated Manufacturing* 2 (3–4) (1985) 237–245.
- [6] Kenneth Falconer, *Fractal Geometry*, John Wiley, New York, 1990.
- [7] B.F. Feeny, G. Lin, Fractional derivatives applied to phase-space reconstructions, *Nonlinear Dynamics* 38 (1–4) (2004) 85–99.
- [8] G. Hovland, S. Hanssen, E. Gallestey, S. Moberg, T. Brogrdh, S. Gunnarsson, M. Isaksson, Nonlinear identification of backlash in robot transmissions, in: *Proc. of the 33rd Int. Symposium on Robotics, ISR 2002*, 2002.
- [9] Miguel F.M. Lima, J.A. Tenreiro Machado, Manuel Crisóstomo, Experimental set-up for vibration and impact analysis in robotics, *WSEAS Transactions on Systems* 4 (5) (2005) 569–576.
- [10] Chengbin Ma, Yoichi Hori, The application of fractional order control to backlash vibration suppression, in: *Proc. of American Control Conference*, 2004, pp. 2901–2906.
- [11] S. Mallat, A theory for multiresolution signal decomposition: The wavelet representation, *IEEE Transactions on Pattern Analysis and Machine Intelligence* 11 (7) (1989) 674–693.
- [12] S. Mallat, *A Wavelet Tour of Signal Processing*, Academic Press, 1999.
- [13] R. Merzouki, J.A. Davila, J.C. Cadiou, L. Fridman, Backlash phenomenon observation and identification, in: *Proc. of American Control Conference*, 2006, pp. 3322–3327.
- [14] Mattias Nordin, Per-Olof Gutman, Non-linear speed control of elastic systems with backlash, in: *Proc. 39th IEEE Conf. on Decision and Control*, 2000, pp. 4060–4065.
- [15] Mattias Nordin, Per-Olof Gutman, Controlling mechanical systems with backlash — a survey, *Automatica* 38 (2002) 1633–1649.
- [16] Heinz-Otto Peitgen, Hartmut Jrgens, Dietmar Saupe, *Chaos and Fractals — New Frontiers of Science*, Springer-Verlag, New York, 2004.
- [17] N. Sarkar, R.E. Ellis, T.N. Moore, Backlash detection in geared mechanisms: Modeling, simulation, and experimentation, *Mechanical Systems and Signal Processing* 11 (3) (1997) 391–408.
- [18] David R. Seidl, Sui-Lun Lam, Jerry A. Putman, Robert D. Lorenz, Neural network compensation of gear backlash hysteresis in position-controlled mechanisms, *IEEE Transactions on Industry Applications* 31 (6) (1995) 1475–1483.
- [19] Claude E. Shannon, A mathematical theory of communication, *The Bell System Technical Journal* 27 (1948) 379–423. 623–656.
- [20] J.L. Stein, Churn-Hway Wang, Automatic detection of clearance in mechanical systems: Theory and simulation, in: *Proc. American Control Conference*, 1995, pp. 1737–1745.
- [21] Chun-Yi Su, Masahiro Oya, Henry Hong, Stable adaptive fuzzy control of nonlinear systems preceded by unknown backlash-like hysteresis, *IEEE Transactions on Fuzzy Systems* 11 (1) (2003) 1–8.
- [22] L. Szabo, J.B. Dobai, K.A. Biro, Chapter Discrete Wavelet Transform Based Rotor Faults Detection Method for Induction Machines, in: *Intelligent Systems at the Service of Mankind*, vol. 2, Ubooks, ISBN: 3-86608-052-2, 2005, pp. 63–74.
- [23] C. Torrence, G.P. Compo, A practical guide to wavelet analysis, *Bulletin of the American Meteorological Society* 79 (1) (1998) 61–78.
- [24] I. Trendafilova, H. Van Brussel, Non-linear dynamics tools for the motion analysis and condition monitoring of robot joints, *Mechanical System and Signal Processing* 15 (6) (2001) 1141–1164.
- [25] James S. Walker, *A Primer on Wavelets and their Scientific Applications*, Chapman & Hall/CRC, 1999.